Ultrafast Electronic Relaxation in Aqueous [Fe(bpy)$_3$]$^{2+}$: A Surface Hopping Study

Satoru Iuchi* and Nobuaki Koga

*Graduate School of Informatics, Nagoya University, Furo-cho, Chikusa-ku, Nagoya 464-8601, Japan*

E-mail: iuchi@i.nagoya-u.ac.jp

1

Abstract

Trajectory surface hopping simulations are performed to better understand the electronic relaxation dynamics of $[Fe(bpy)_3]^{2+}$ in aqueous solution. Specifically, the ultrafast relaxation from the photo-excited singlet metal-to-ligand charge-transfer (MLCT) to the metastable quintet metal-centered (MC) states is simulated through the surface hopping method, where the MLCT and MC states of $[Fe(bpy)_3]^{2+}$ in aqueous solution are computed by using a model electronic Hamiltonian developed previously. As a result, most of the trajectories are interpreted to show the sequential relaxation pathways via the triplet MC states, though some are the direct pathway from MLCT to the quintet MC states. In spite that the triplet MC states are involved in the relaxation, the population transfer to the singlet MC ground state is very small and the population of the quintet MC states reaches more than $\sim 96\%$, reasonably consistent with the unity quantum efficiency discussed experimentally.

TOC Graphic
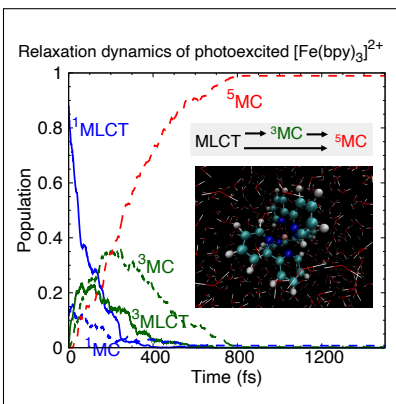
Electronic relaxation dynamics of transition metal complexes has been an important research subject in physical chemistry because understanding of the relaxation processes is important not only for fundamental concepts but also for potential applications such as solar energy conversion.[1–5] For example, the ultrafast intersystem crossing (ISC) process of a prototypical iron(II) polypyridyl complex, $[Fe(bpy)_3]^{2+}$ (bpy=2,2′-bypiridine), has been experimentally studied[6–13] to clarify the relaxation from the photo-excited singlet metal-to-ligand charge-transfer (^{1}MLCT) states to the metastable quintet $^5T_{2g}$ states, where T_{2g} represents the metal-centered (MC or d-d) states labeled by the O_h symmetry. Advanced wavefunction-based ab initio calculations have been also utilized to reveal mechanism of this ultrafast ISC in detail.[14–18] Quantum-mechanical theories with the simplified picture of the electronic structure for iron(II) complexes have been also utilized to investigate the mechanism in more general sense.[19,20] For the prototypical $[Fe(bpy)_3]^{2+}$ complex, two mechanisms have been mainly discussed: the direct MLCT→$^5T_{2g}$ transition[7,10] and the sequential transitions via the intermediate triplet MC states ($^3T_{2g}$ and $^3T_{1g}$).[9] The involvement of two mechanisms has been also discussed both experimentally[11] and theoretically.[18]

To understand this non-equilibrium process more clearly, non-adiabatic simulations based on electronic structure theory calculations are also meaningful. However, to perform such non-adiabatic simulations for ISCs in transition metal complexes, various issues have to be taken into account in general. Potential energies of multiple excited states including different spin multiplicities have to be computed, requiring wavefunction-based ab initio methods to include large electron correlation effects. Spin-orbit (SO) and non-adiabatic couplings have to be also computed during simulations. Moreover, relatively large number of vibrational degrees of freedom should be considered because reaction coordinates to describe relaxation processes are not always clear in advance. Therefore, various methods have been developed to take account of these issues in performing non-adiabatic simulations for transition metal complexes.[4,21,22] The trajectory surface hopping (SH) method with the linear vibronic coupling (LVC) model is an example to simulate the ultrafast ISCs in transition metal com-

plexes,[22] where a full dimensional potential energy surface is provided by the LVC Hamiltonian parameterized using the harmonic oscillators of the ground state and the intrastate and interstate coupling terms. The SH simulations using LVC have been performed for transition metal systems,[22] including one of the iron(II) polypyridyl complexes, $[\text{Fe(terpy)}_2]^{2+}$ (terpy=2,2′:6′,2″-terpyridine).[23]

On the other hand, a model effective Hamiltonian approach developed by us[24,25] also provides information on a full dimensional potential energy surface of $[\text{Fe(bpy)}_3]^{2+}$.[25–28] The model Hamiltonian matrix of $[\text{Fe(bpy)}_3]^{2+}$ is constructed by using all the electronic configurations arising from $(3\text{d})^6$ and $(3\text{d})^5(\pi^*)^1$ as basis functions. The matrix elements are modeled by physically reasonable functions with proper parameters so that the model Hamiltonian provides reasonable information on both MLCT and MC states in a computationally cheap fashion.[28] In this study, to better understand the ultrafast ISC of $[\text{Fe(bpy)}_3]^{2+}$ in aqueous solution, trajectory SH simulations using this model Hamiltonian[28] are performed. The use of the model Hamiltonian as an alternative of first principle electronic structure calculations is a compromise in terms of the accuracy. However, the present emphasis is to obtain insights into the relaxation mechanism by explicitly dealing with the multiple excited states and all the nuclear degrees of freedom. Note that the wavepacket quantum dynamics simulations based on 9 selected vibrational modes have been recently performed for the isolated $[\text{Fe(bpy)}_3]^{2+}$ to explore the relaxation mechanism.[29]

The model effective Hamiltonian of $[\text{Fe(bpy)}_3]^{2+}$ is described in the previous study,[28] and the details pertinent to this study are briefly outlined here. The basis functions (all the $(3\text{d})^6$ and $(3\text{d})^5(\pi^*)^1$ configurations) of the model effective Hamiltonian matrix $\boldsymbol{H}_{\text{eff}}$ are expressed by the Slater determinants Φ composing of the metal 3d atomic orbitals and model orbitals to represent ligand π^*, where the 3d and π^* are assumed to be orthogonal. The model Hamiltonian matrix is written as the sum of the metal (M) d-electron repulsion,

the metal-ligand (M–L) interaction, and the ligand (L) interaction matrices as

$$\boldsymbol{H}_{\text{eff}} = \boldsymbol{H}_{\text{M}} + \boldsymbol{H}_{\text{ES}} + \boldsymbol{H}_{\text{EX}} + \boldsymbol{H}_{\text{CT}} + \boldsymbol{H}_{\text{L}} \tag{1}$$

where ES, EX, and CT represent the M–L electrostatic, exchange, and charge-transfer interactions, respectively. The appropriate functional forms of these matrix elements are modeled as the two-electron and one-electron terms for M and M–L, respectively. The $\boldsymbol{H}_{\text{L}}$ matrix is diagonal because the ligands are modeled by the general Amber force field.[30] Note that solvents can be also included in the L related terms, and effects of waters are included in the ES term through a flexible water force field. The SO matrix $\boldsymbol{H}_{\text{SO}}$ is further computed by defining a one-electron SO operator, $\hat{H}_{\text{SO}} = \zeta_{\text{SO}} \sum_{i=1}^{6} \hat{\boldsymbol{l}}_i \cdot \hat{\boldsymbol{s}}_i$ with a constant parameter ζ_{SO}. The spin-mixed states are computed by diagonalizing $\boldsymbol{H}_{\text{eff}} + \boldsymbol{H}_{\text{SO}}$ as

$$\mathscr{E}(\boldsymbol{R}) = \boldsymbol{d}(\boldsymbol{R})^{\dagger} \left(\boldsymbol{H}_{\text{eff}}(\boldsymbol{R}) + \boldsymbol{H}_{\text{SO}} \right) \boldsymbol{d}(\boldsymbol{R}) \tag{2}$$

where $\mathscr{E}$ is a diagonal matrix containing the electronic energies of the spin-mixed states. The $\boldsymbol{H}_{\text{SO}}$ matrix is independent of the nuclear coordinates $\boldsymbol{R}$ due to the aforementioned operator form. The wave function of the s-th spin-mixed state is written as a linear combination of Φ as

$$|\Xi_s(\boldsymbol{r}; \boldsymbol{R})\rangle = \sum_{I=1}^{N_{\text{det}}} d_{Is}(\boldsymbol{R}) |\Phi_I(\boldsymbol{r}; \boldsymbol{R})\rangle \tag{3}$$

where $\boldsymbol{r}$ are the electronic coordinates and the number of the Slater determinants (N_{det}) is 1722: 210 $(3d)^6$ and 1512 $(3d)^5(\pi^*)^1$ configurations. The expression of the forces, used to propagate nuclear positions and velocities in simulations, is derived from eq 2 according to the Hellmann-Feynman theorem.

In the SH simulations, the time-dependent electronic wave function is written as a linear combination of Ξ as

$$|\Theta(t)\rangle = \sum_{s} c_s(t) |\Xi_s(\boldsymbol{r}; \boldsymbol{R}(t))\rangle \tag{4}$$

and the time-dependent coefficients, $\boldsymbol{c}(t)$, are propagated along the classical molecular dynamics (MD) trajectory $\boldsymbol{R}(t)$ by

$$\boldsymbol{c}(t + \Delta t) = \exp\left[-\int_t^{t+\Delta t}\left(\frac{i}{\hbar}\{\boldsymbol{H}_{\text{eff}}(\tau) + \boldsymbol{H}_{\text{SO}}(\tau)\} + \boldsymbol{T}(\tau)\right)d\tau\right]\boldsymbol{c}(t) \tag{5}$$

which is derived by inserting eq 4 into the time-dependent electronic Schrödinger equation. The derivative couplings $T_{rs}(t) = \langle\Xi_r(\boldsymbol{r};\boldsymbol{R}(t))\left|\frac{\partial}{\partial t}\right|\Xi_s(\boldsymbol{r};\boldsymbol{R}(t))\rangle$ can be analytically evaluated by using the wave functions (eq 3). However, in the present target system, many spin-mixed states are likely to be weakly coupled through the SO couplings especially around the Franck-Condon region because various spin-free states are relatively close in energy as seen in the potential energy curves along a symmetric $[\text{Fe(bpy)}_3]^{2+}$ distortion in Figure 1. Therefore, the derivative couplings are expected to be strongly localized and overlooked unless MD time step Δt is very small.[31] To deal with such situations with a larger Δt, the propagation of $\boldsymbol{c}(t)$ is performed by the three-step propagator in the surface hopping including arbitrary couplings (SHARC) approach,[32,33] with the local diabatization method.[34]
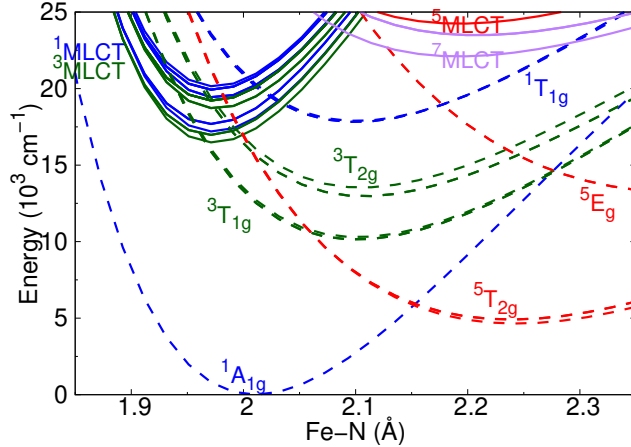

Figure 1: Potential energy curves of selected low-lying spin-free states (eqs 6 and 7) along the interpolation/extrapolation between the D_3 symmetric $^1\text{A}_1$ and $^5\text{A}_1$ optimized structures of $[\text{Fe(bpy)}_3]^{2+}$. The MLCT and the MC (labeled by the O_h symmetry) states are displayed by solid and dashed lines, respectively. Drawn by using the data computed by the model Hamiltonian in the previous study.[28]

Specifically, in addition to the spin-mixed states (eqs 2 and 3), the spin-free states are

computed along the classical MD trajectory by diagonalizing the model Hamiltonian as

$$\boldsymbol{E}(\boldsymbol{R}(t)) = \boldsymbol{C}(\boldsymbol{R}(t))^{\dagger}\boldsymbol{H}_{\text{eff}}(\boldsymbol{R}(t))\boldsymbol{C}(\boldsymbol{R}(t)) \tag{6}$$

where $\boldsymbol{E}$ is a diagonal matrix containing the electronic energies of the spin-free states. The wave function of the n-th spin-free state is thus given as

$$|\Psi_n(\boldsymbol{r}; \boldsymbol{R}(t))\rangle = \sum_{I=1}^{N_{\text{det}}} C_{In}(\boldsymbol{R}(t)) |\Phi_I(\boldsymbol{r}; \boldsymbol{R}(t))\rangle \tag{7}$$

The spin multiplicities $2S + 1$ and the projected values M_S can be determined clearly (no spin contamination) from the expectation values of the spin operators $\hat{S}^2$ and $\hat{S}_z$ by using eq 7. Then, the matrix $\boldsymbol{H}^{\text{MCH}} = \boldsymbol{E} + \boldsymbol{H}^{\text{MCH}}_{\text{SO}}$ is constructed by using Ψ as the basis functions, where the notation MCH (molecular Coulomb Hamiltonian) is employed as in the SHARC approach.[32,33] The electronic energies of the spin-mixed states computed by diagonalizing this matrix

$$\mathscr{E}(\boldsymbol{R}(t)) = \boldsymbol{U}(\boldsymbol{R}(t))^{\dagger}\boldsymbol{H}^{\text{MCH}}(\boldsymbol{R}(t))\boldsymbol{U}(\boldsymbol{R}(t)) \tag{8}$$

are equal to those from eq 2, but the wave function of the s-th spin-mixed state is here written in terms of the spin-free states as

$$|\Xi_s(\boldsymbol{r}; \boldsymbol{R}(t))\rangle = \sum_{n=1}^{N_{\text{state}}} U_{ns}(\boldsymbol{R}(t)) |\Psi_n(\boldsymbol{r}; \boldsymbol{R}(t))\rangle \tag{9}$$

The propagation of the time-dependent coefficients $\boldsymbol{c}(t)$ is based on the three-step propagator,[32,33] where $\boldsymbol{U}$, $\boldsymbol{H}^{\text{MCH}}$, and the overlap matrix $\boldsymbol{S}^{\text{MCH}}(t, t + \Delta t)$ are utilized. The overlaps $S_{mn}^{\text{MCH}}(t, t + \Delta t) = \langle \Psi_m(\boldsymbol{r}; \boldsymbol{R}(t)) | \Psi_n(\boldsymbol{r}; \boldsymbol{R}(t + \Delta t)) \rangle$ are used to locally diabatize $\boldsymbol{H}^{\text{MCH}}$. The further details including the actual numerical procedures are summarized in Supporting Information, Section S2.4.

To prepare for the photo-excited states at $t = 0$, the absorption cross section $\sigma(\omega)$

7

was computed by the oscillator strengths and vertical excitation energies of the spin-mixed states at 2000 solvated configurations as shown in Figure 2. By the similar procedure as in literature,[35] these configurations were prepared by generating 2000 $[Fe(bpy)_3]^{2+}$ complex structures according to the Wigner distribution based on the normal coordinates at the ground $^1A_{1g}$ state, and only water solvents were equilibrated by a NVT simulation with the complex coordinates being frozen. For comparison, the spectra were also computed in gas phase by using the same 2000 $[Fe(bpy)_3]^{2+}$ complex structures. As observed in Figure 2, the first peak in aqueous solution is lower in wavenumber than that in gas phase, implying the solvents stabilize the low-lying MLCT states when the complex is distorted from the symmetric structure. To see this further, five $[Fe(bpy)_3]^{2+}$ structures including water molecules in the first solvation shell were sampled from the equilibrium MD simulation. The computed excitation energies at these structures with and without water molecules (Table S1) show that the solvents do not affect the excitation energies of low-lying MC states whereas the excitation energies of low-lying MLCT states are lowered by solvents: average shift of three low-lying MLCT states (15 states in total) is 638 cm^{-1}. The similar tendency was reported in the CASPT2 calculations using the polarizable continuum model,[17] supporting that the solvent effects are qualitatively properly included in the model Hamiltonian with the water force field.

The first peak in the absorption spectrum is located at $\sim$18000 cm^{-1} (Figure 2), which is lower by $\sim$1000 cm^{-1} than that of $\sim$19000 cm^{-1} in the experimental spectrum.[6,9] Considering the experimental excitations of 580 nm (17241 cm^{-1})[10] and 520 nm (19231 cm^{-1}),[9] the excitation energies were set to 16250$\pm$750 (case 1) and 18250$\pm$500 cm^{-1} (case 2). In these energy regions, 107 and 131 initial excited states were selected, respectively, based on a stochastic algorithm.[36] In this study, the excitations were additionally restricted to the excited states dominated by the singlet character. Details of the initial excited states selection are summarized in Section S2.2.

The SH simulations were performed from these initial excited states. The nuclear po-
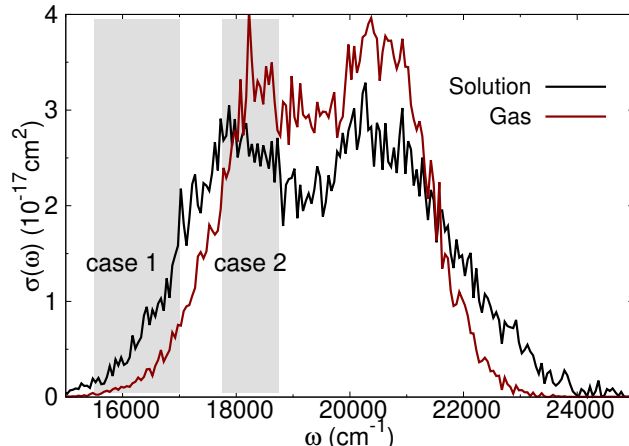
Figure 2: Absorption cross section $\sigma(\omega)$ computed by using 2000 solvated configurations. Gray areas represent the energy regions where the initial excited states were selected. For a comparison, the spectrum computed by using the same 2000 structures in gas phase are also shown (dark-red line).

sitions $\boldsymbol{R}(t)$ and velocities $\boldsymbol{v}(t)$ were propagated for 1500 fs with Δt of 0.5 fs without the thermostat, whereas $\boldsymbol{c}(t)$ were propagated with a time step of 0.02 fs. The periodic system is composed of one $[\text{Fe}(\text{bpy})_3]^{2+}$ and 890 waters in the cubic unit cell. The hopping probabilities proposed in the SHARC approach[32,33] were computed at $t + \Delta t$ to judge whether the hop to the new state occurs. When a hop was decided, $\boldsymbol{v}(t+\Delta t)$ of only $[\text{Fe}(\text{bpy})_3]^{2+}$ were scaled to maintain the total energy of the system. Finally, an energy-based decoherence correction[37] was applied for $\boldsymbol{c}(t + \Delta t)$. All the calculations were performed with a program modified from DL_POLY 2.20,[38] where the model Hamiltonian and the present SH procedures were implemented. The further details of these computations are given in Sections S2.1 and S2.4.

The populations in the MCH (spin-free) representation are examined because these can be interpreted more easily than those in the spin-mixed representation.[32,33] However, the result is still difficult to be interpreted because many spin-free states are involved (see the populations in Figure S1). Therefore, the MCH populations summed over all the singlet, triplet, and quintet contributions were evaluated (eq S13), where the MCH populations were decomposed into the MLCT and MC contributions by using the MLCT and MC weights (eqs S14 and S15). As seen in Figure 3, the ^{1}MLCT populations decrease to ~ 0.2 within

9

200 fs, whereas the ^{5}MC populations are more than 0.96 at 1.5 ps, irrespective of the initial excitations. These results are reasonably consistent with the ultrafast deactivation to ^{5}T$_{2g}$ with the unity quantum efficiency discussed experimentally,[7,10] supporting the present model Hamiltonian approach.
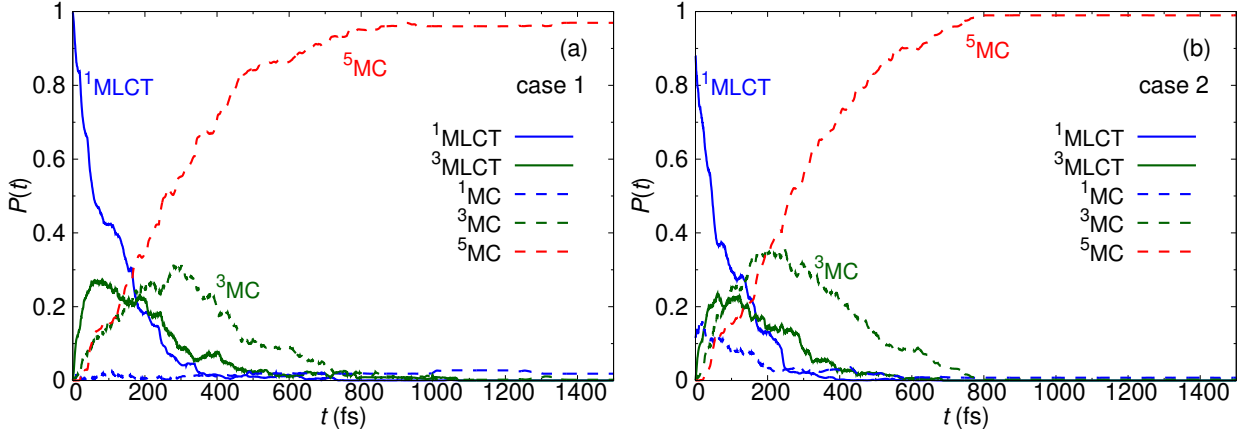

Figure 3: MLCT and MC populations $P_{2S+1}^k(t)$ (eq S13) after photo-excitations of (a) case 1 and (b) case 2 in Figure 2. The ^{5}MLCT contributions are less than 0.01 and not shown.

It is also apparent in Figure 3 that both the ^{3}MLCT and ^{3}MC are populated during the relaxation. The rapid population transfer to ^{3}MLCT is consistent with the ISC transition timescale of 28 fs evaluated by the Fermi's golden rule using DFT and CASPT2 calculations in ref 16. By contrast, the slower increase of the ^{3}MC population is observed in Figure 3, though the ^{1}MLCT$\rightarrow$^{3}T$_{2g}$ transition was predicted to be as fast as ^{1}MLCT$\rightarrow$^{3}MLCT in the Fermi's golden rule analysis.[16] In the present model Hamiltonian, the SO couplings between the MLCT and MC states are modeled only by the mixings of MLCT and MC characters (no mixings between the 3d and π^* orbitals in Φ) and thus may be underestimated when the MLCT and MC states are relatively separated in energy.[28] In this regard, it is not conclusive as to whether the ^{1}MLCT$\rightarrow$^{3}T$_{2g}$ pathway plays a relatively minor role. The ^{5}MLCT populations were found to be less than 0.01, indicating that the ^{5}MLCT states are not involved in the mechanism.

Each population in Figure 3 is given as a sum of a few different spin-free state contributions; for example, the ^{5}MC population may include both the ^{5}T$_{2g}$ and ^{5}E$_g$ contributions.

10

Therefore, to obtain the further insights, all spin-free states were assigned to either MLCT or MC based on the weights of electronic configurations ($|C_{In}|^2$ in eq 7) and classified into $^1A_{1g}$, $^1T_{1g}$, $^3MC_1$, $^3MC_2$, $^5T_{2g}$, ^5E_g, ^1MLCT, and ^3MLCT (see the procedure in Section S1). Note that there is ambiguity in distinguishing $^3T_{1g}$ and $^3T_{2g}$ in particular due to the possible mixings of these states at distorted structures. Therefore, low-lying six triplet MC states (18 states including the M_S substates), simply assigned by the order in energy, were labeled by $^3MC_1$ and $^3MC_2$ hereafter, as adopted in the study on a V(III) complex.[39] Because each electronic state can be a mixture of the MLCT and MC characters and the complex structure is not symmetric during simulations, the results based on the present state assignments should be taken as rough pictures. Figure 4 shows the populations of these states, where it is seen that the ^1MLCT populations rapidly decay and the maxima of the ^3MLCT, $^3MC_2$, and $^3MC_1$ populations appear in this order, irrespective of the initial excitations. These characteristics imply the existence of the sequential pathways to $^5T_{2g}$ via $^3MC_{1,2}$, though the direct MLCT$\rightarrow^5T_{2g}$ pathway may coexist. To clarify this issue, the populations were analyzed along the trajectories as in the SH study for [Fe(terpy)$_2$]$^{2+}$.[23] To see the analyzed results clearly, the most populated state along each trajectory was tracked[39] as shown in Figure 5. As a result, it is interpreted that both the sequential pathways via $^3MC_2$ and/or $^3MC_1$ and the direct MLCT$\rightarrow^5T_{2g}$ pathway exist. For example, the 6-th and 9-th (case 1), and the 3-rd and 11-th (case 2) trajectories are interpreted to show the sequential pathways, whereas the 1-st (case 1) and 7-th (case 2) trajectories are the direct pathway. The relaxations in the individual trajectories were roughly classified into ten types as summarized in Table 1. Although there are some ambiguities in these classifications due to multiple state changes in trajectories, the present classifications are rationalized by the populations along the above-mentioned six trajectories as shown in Figure S3. It is clear from this analysis that the sequential pathways from MLCT via $^3MC_2$ and/or $^3MC_1$ are dominant: 61 and 78 trajectories were classified into one of the sequential changes for the cases 1 and 2, respectively. On the other hand, non-negligible trajectories (36 and 25 for the cases 1 and 2) were

classified into the direct MLCT→^{5}T$_{2g}$ change. Therefore, it is reasonable to interpret that both the sequential and direct pathways coexist in the relaxation process of [Fe(bpy)$_3$]$^{2+}$. This is rationalized by considering that the ^{1,3}MLCT and ^{5}T$_{2g}$ states are relatively close in energy (Figure 1) and expected to be strongly mixed. Note that the similar analyses applied to the populations in Figure 3 resulted in qualitatively the same results: 65 and 67 trajectories were classified into the sequential MLCT→^{3}MC→^{5}MC, and 35 and 27 trajectories to the direct MLCT→^{5}MC for the cases 1 and 2, respectively. Therefore, the aforementioned rough MLCT/MC assignments do not affect the present discussions qualitatively.
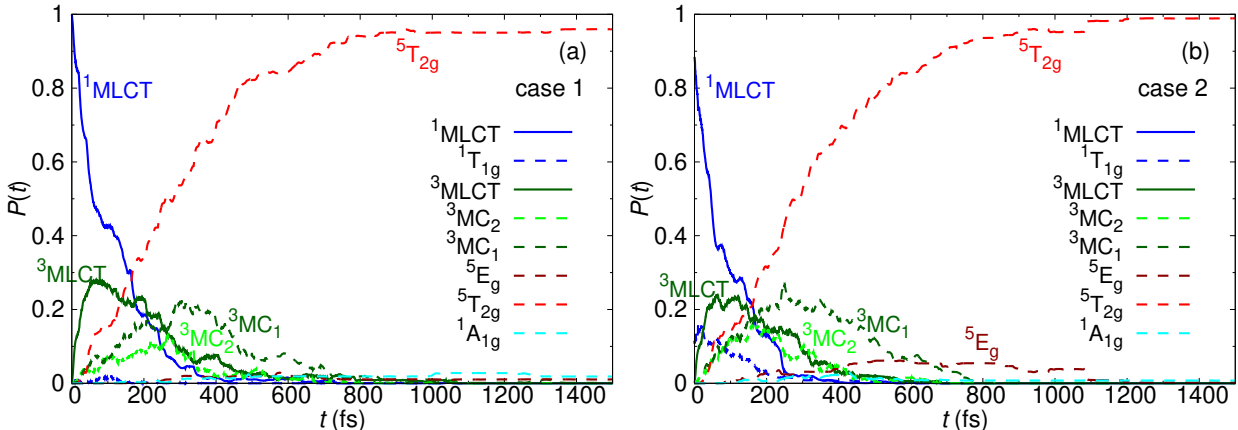

Figure 4: Populations classified into various contributions $P_n(t)$ (eq S12) after photo-excitations of (a) case 1 and (b) case 2 in Figure 2. The subscript n denotes ^{1,3}MLCT (solid) and ^{1}A$_{1g}$, ^{1}T$_{1g}$, ^{3}MC$_1$, ^{3}MC$_2$, ^{5}T$_{2g}$, and ^{5}E$_g$ (dashed), respectively.

As seen in Table 1, among five types of the sequential pathways, the cascade-like process, MLCT→^{3}MC$_2$→^{3}MC$_1$→^{5}T$_{2g}$, is dominant for both the cases 1 and 2, followed by the MLCT→^{3}MC$_1$→^{5}T$_{2g}$ one. By contrast, the MLCT→^{3}MC$_2$→^{5}T$_{2g}$ pathway is very minor. The efficient population transfer from MLCT to ^{3}MC$_1$ is rationalized by considering that these states are close in energy at the Franck-Condon region as seen in Figure 1. The characteristics of the population transfers based on the present assignments would be useful to obtain insights into the relaxation process. The potential energy curves in Figure 1 show that ^{3}T$_{2g}$ (i.e., ^{3}MC$_2$) and ^{3}T$_{1g}$ (i.e., ^{3}MC$_1$) are separated in energy along a symmetric [Fe(bpy)$_3$]$^{2+}$ distortion. However, due to the surface crossing associated with the distorted

Table 1: Classifications of relaxation pathways in individual trajectories based on most populated states along trajectories in Figure 5.[a]

pathway type	case 1	case 2	pathway[b]
type 1 (sequential)	35	33	MLCT$\rightarrow^3$MC$_2\rightarrow^3$MC$_1\rightarrow^5$T$_{2g}$
type 2 (sequential)	2	2	MLCT$\rightarrow^3$MC$_2\rightarrow^5$T$_{2g}$
type 3 (sequential)	23	27	MLCT$\rightarrow^3$MC$_1\rightarrow^5$T$_{2g}$
type 4 (sequential)	1	16	MLCT$\rightarrow^1$T$_{1g}\rightarrow^3$MC$_2\rightarrow^3$MC$_1\rightarrow^5$T$_{2g}$ [c]
type 5 (sequential)	0	1	^{1}T$_{1g}\rightarrow^3$MC$_2\rightarrow^3$MC$_1\rightarrow^5$T$_{2g}$
type 6 (direct)	36	25	MLCT$\rightarrow^5$T$_{2g}$
type 7 (other)	2	11	pathways involving ^{5}E$_g$ (^{1}A$_{1g}$ is not involved.)
type 8 (other)	3	10	pathways involving ^{1}A$_{1g}$ (^{5}E$_g$ are not involved.)
type 9 (other)	1	5	other pathways which reach ^{5}T$_{2g}$
others	4	1	other pathways which do not reach ^{5}T$_{2g}$
total	107	131	

[a] The regions where the most populated state was not determined (white color region in Figure 5) were neglected in assigning the pathway.
[b] Trajectories containing the characters of two types were assigned to a pathway including more states. For example, the trajectories 7 (case 1) and 8 (case 2) were assigned to the type 3 and 1, respectively, though they contain the type 6 character around 225 and 25 fs, respectively. In addition, each pathway sometimes includes multiple state changes; for example, the trajectory 3 (case 2) assigned to type 4 contains ^{3}MC$_1\rightarrow^5$T$_{2g}\rightarrow^3$MC$_1\rightarrow^5$T$_{2g}$ as seen in Figure S3d.
[c] ^{1}T$_{1g}\rightarrow$MLCT$\rightarrow^1$T$_{1g}\rightarrow^3$MC$_2\rightarrow^3$MC$_1\rightarrow^5$T$_{2g}$ and ^{1}T$_{1g}\rightarrow$MLCT$\rightarrow^3$MC$_2\rightarrow^3$MC$_1\rightarrow^5$T$_{2g}$ were also assigned to this type.
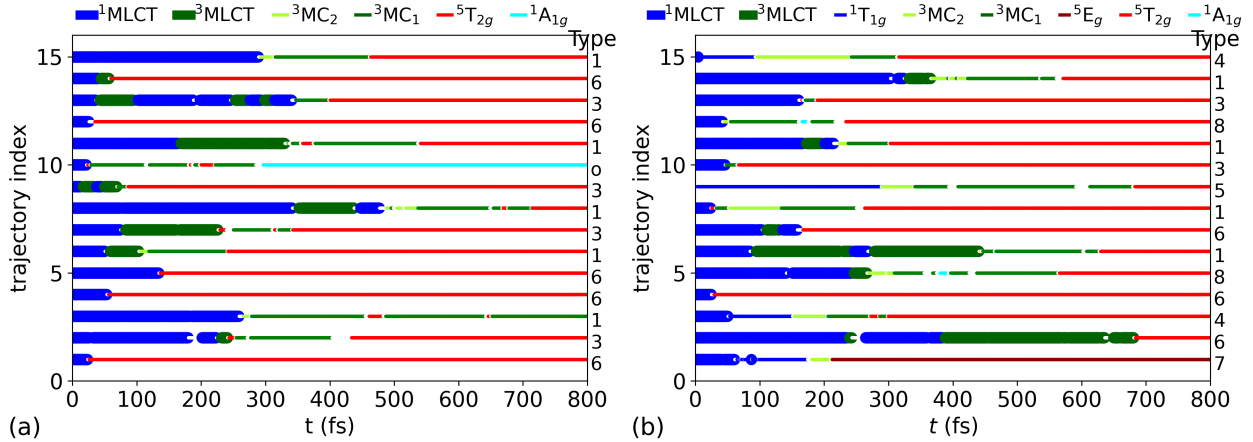
Figure 5: The most populated state along trajectories after photo-excitations of (a) case 1 and (b) case 2 in Figure 2. For clarity, only the results of 15 trajectories up to 800 fs are shown: results for all the trajectories up to 1500 fs are shown in Figure S2. The most populated states are labeled by different sizes and colors as shown in legend. White color region corresponds to the case when the population of the most dominant state is less than 0.6. Numbers displayed in the right side denote the assigned pathway types defined in Table 1.

motions, the internal conversion $^3MC_2 \rightarrow {}^3MC_1$ was shown to be plausible with a timescale of $\sim$100 fs in the previous equilibrium MD simulation using the model Hamiltonian,[27] consistent with the the cascade-like process mentioned above. Similarly, although the $^3T_{1g}$ (i.e., $^3MC_1$) and $^1A_{1g}$ are separated in energy along the symmetric distortion as seen in Figure 1, this is not the case around the equilibrium for $^3MC_1$. In the previous equilibrium MD simulations for $^3MC_1$, the lowest $^3MC_1$ becomes close to both $^5T_{2g}$ and $^1A_{1g}$ in energy, strongly implying that the $^3MC_1 \rightarrow {}^1A_{1g}$ transition cannot be ruled out if the equilibrium of $^3MC_1$ is assumed.[27,28] However, the present results in Figure 4 indicate that the population transfer to $^1A_{1g}$ is inefficient during the non-equilibrium process and hence nearly all the populations are finally transferred to $^5T_{2g}$ even when the intermediate $^3MC_{1,2}$ states are involved: only 4 and 1 trajectories did not reach the $^5T_{2g}$ states for cases 1 and 2, respectively, as summarized in Table 1.

In an experimental study,[10] the direct MLCT$\rightarrow {}^5T_{2g}$ process was discussed, which can explain the unity quantum efficiency because the involvement of the $^3T_{2g,1g}$ states would lead

14

to some leakage to the ground $^1A_{1g}$ state. However, the population transfer to $^1A_{1g}$ can be very minor even if the intermediate $^3MC_{1,2}$ states are involved as shown above. Therefore, coexisting the direct and sequential pathways interpreted from the present simulations does not indicate a clear contradiction to the unity quantum efficiency. As for the $^1T_{1g}$ and ^5E_g states, these populations are very small during the relaxation for the case 1, but not negligible for the case 2, as seen in Figure 4. This is rationalized by considering that the ^1MLCT and $^1T_{1g}$ states are separated in energy at the Franck-Condon region in the case 1, whereas those could be mixed and the upper lying ^5E_g could be also populated due to the higher excitation energy in the case 2 (Figure 1). Nevertheless, two simulation results indicate that irrespective of such details $^5T_{2g}$ is populated by more than ∼96% eventually.

Finally, the present results are compared to those in the relevant simulation studies. In the recent SH simulation study of the isolated $[Fe(terpy)_2]^{2+}$, the populations along the representative trajectories were analyzed to identify the pathways.[23] In both this and the present SH studies, the sequential pathway involving ^3MC was found, supporting the viewpoint that the involvement of ^3MC is a common characteristics of the relaxations in the iron(II)-polypyridyl complexes. However, in the simulation study of $[Fe(terpy)_2]^{2+}$, the $^3MLCT \rightarrow ^3T_{2g} \rightarrow ^5T_{2g}$ pathway was also found instead of $^3MLCT \rightarrow ^3T_{1g} \rightarrow ^5T_{2g}$. In addition, the role of the direct $MLCT \rightarrow ^5T_{2g}$ process was concluded to be negligible. These points are different from the present results. In the wavepacket quantum dynamics study of the isolated $[Fe(bpy)_3]^{2+}$,[29] the possibility of the direct pathway was excluded, and the $^3T_{1g}$ was discussed to be the main intermediates. These details are also different from the present results. However, the relative energies among three different spin multiplicities are sensitive to the details of the models. For example, the vertical excitation energies to $^3T_{2g}$ lie in a range of 15599-16042 and 19438-21132 cm^{-1} for the present model[28] and the model in ref 29, respectively. Therefore, the differences appeared in the details of the computed pathways may originate from the differences of computed potential energy surfaces such as the locations of the crossing points of $MLCT/^5T_{2g}$ and $MLCT/^3MC$, though further investigations

are necessary to confirm this. Note that in the wavepacket quantum dynamics study,[29] the bpy C2–C2′ stretching was shown to play a role in the ISC process. Similarly, identifying the active normal modes which drive the deactivations is also necessary in the present simulation study, which remains an important issue to be studied.

In the time-resolved ultrafast spectroscopies, vibrational wavepackets were observed, which have been attributed to the Fe–N related modes of $[Fe(bpy)_3]^{2+}$.[8,10,12] To examine the wavepacket motions associated with the transitions to $^5T_{2g}$, the changes of the average Fe–N bond length were computed for simplicity. As observed in Figure 6 (solid lines), the average Fe–N bond lengths are $\sim$2.3 Å after around 500 fs, whereas those are 1.998 (case 1) and 2.012 (case 2) Å initially. This is ascribed to a consequence of the deactivation to $^5T_{2g}$ because the average Fe–N bond lengths were computed to be 2.027 and 2.291 Å in the equilibrium MD simulations for $^1A_{1g}$ and the lowest $^5T_{2g}$, respectively.[28] However, in the present result, oscillation behaviors are not distinctive: only a small oscillation behavior seems to appear for the case 1. It is tentatively interpreted that solute-solvent interactions are overemphasized in the present model Hamiltonian and thus the Fe–N oscillations are not distinctive due to the overemphasized decoherence in aqueous solution. It was suggested that the ^3T states can contribute to the decoherence,[12] and thus a small oscillation behavior for the case 1 is rationalized by considering that the direct MLCT$\rightarrow^5T_{2g}$ pathway is relatively more frequent in the case 1 than in the case 2 as observed in Table 1.

To further examine whether the lack of the Fe–N oscillation behaviors is a consequence of other deficiencies of the present model Hamiltonian, the trajectory SH simulations were also performed in gas phase (Section S2.4.5). This is motivated by the recent SH simulation study for the isolated $[Fe(terpy)_2]^{2+}$, where coherent oscillations of Fe–N are observed.[23] As shown in Figure 6, Fe–N oscillation behaviors are distinctive in the gas phase simulations. These oscillations are indeed ascribed to the motions associated with the transitions to $^5T_{2g}$, because similar oscillation periods were observed from the non-equilibrium MD simulations with respect to the lowest $^5T_{2g}$ spin-free state (Figure S8), where the same initial coordinates
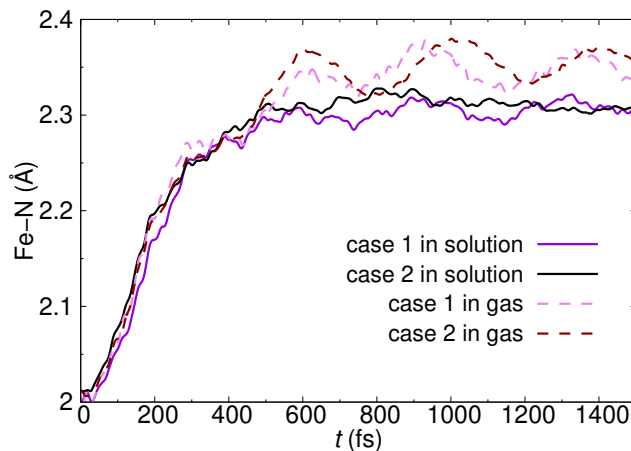
Figure 6: Changes of average Fe–N bond length averaged over trajectories after photo-excitations of the cases 1 and 2 in Figure 2 (aqueous solution) and in Figure S4 (gas phase).

and velocities in the SH simulations were used.

In the gas phase SH simulations, the main characteristics in the time-evolution of populations (Figures S5 and S6) are qualitatively similar with those discussed above for the aqueous system in Figures 3 and 4. On the other hand, the details of the pathways are different as summarized in Table S2, where the numbers of the direct pathway are found to be smaller than those in aqueous solution (Table 1). This result seems to be related with the possible overestimation of solute-solvent interactions mentioned above. The solute-solvent interactions may influence the relative energies among the MLCT and MC states, because the diagonal and some off-diagonal elements of the model Hamiltonian are affected by solvents. Therefore, the MLCT and MC states may have more chances to become close in energy in aqueous solution than in gas phase. In this regard, solvents would facilitate mixing between the MLCT and MC characters, resulting in the increase of the direct transition character. However, a comparison among the results of present four SH simulations also implies that the details of the pathways could be sensitive to the excitations and environments.

To conclude, the ultrafast relaxation from the photoexcited ^{1}MLCT to the metastable ^{5}T$_{2g}$ states in the aqueous [Fe(bpy)$_3$]$^{2+}$ system was explored through the trajectory SH simulations using the model Hamiltonian developed previously. The simulation results indicate that the pathways involving the ^{3}MC states are major, though the character of the direct

MLCT$\rightarrow^5$T$_{2g}$ process also coexists to some extent in the relaxation. Importantly, it is observed in the simulation results that the population transfers from the ^{3}MC states to the singlet ground MC state are very minor and thus the majority of the population finally transfer to ^{5}T$_{2g}$. A comparison to the other SH simulation result for [Fe(terpy)$_2$]$^{2+}$ [23] supports that the existence of pathways involving the ^{3}MC states is a common characteristics in iron(II) polypyridyl complexes. However, it was also implied that the details of the pathways could be sensitive to the excitations and environments because multiple excited states are involved in the process. Therefore, it is likely that the details of pathways could be sensitive to models or quantum chemical calculations employed. In this regard, to clarify the mechanism further, it would be meaningful to perform more simulations with other approaches and compare simulation results.

Acknowledgement

Supporting Information Available

Description of notations and assignments of electronic states, details of computational methods including MD simulations, selection of initial excited states, SH simulations, and analyses, tables and figures of additional data including solvent effects on vertical excitation energies, populations of low-lying states, pathway analyses for all the trajectories, populations of representative trajectories, and results from simulations in gas phase (PDF).

References

(1) Chergui, M. On the Interplay between Charge, Spin and Structural Dynamics in Transition Metal Complexes. *Dalton Trans.* **2012**, *41*, 13022–13029.

(2) Chergui, M. Ultrafast Photophysics of Transition Metal Complexes. *Acc. Chem. Res.* **2015**, *48*, 801–808.

(3) Sousa, C.; Alías, M.; Domingo, A.; de Graaf, C. Deactivation of Excited States in Transition-Metal Complexes: Insight from Computational Chemistry. *Chem. Eur. J.* **2019**, *25*, 1152–1164.

(4) Daniel, C. Ultrafast Processes: Coordination Chemistry and Quantum Theory. *Phys. Chem. Chem. Phys.* **2021**, *23*, 43–58.

(5) Cebrián, C.; Pastore, M.; Monari, A.; Assfeld, X.; Gros, P. C.; Haacke, S. Ultrafast Spectroscopy of Fe(II) Complexes Designed for Solar-Energy Conversion: Current Status and Open Questions. *ChemPhysChem* **2022**, *23*, e202100659.

(6) Gawelda, W.; Cannizzo, A.; Pham, V.-T.; van Mourik, F.; Bressler, C.; Chergui, M. Ultrafast Nonadiabatic Dynamics of $[Fe^{II}(bpy)_3]^{2+}$ in Solution. *J. Am. Chem. Soc.* **2007**, *129*, 8199–8206.

(7) Bressler, C.; Milne, C.; Pham, V.-T.; ElNahhas, A.; van der Veen, R. M.; Gawelda, W.; Johnson, S.; Beaud, P.; Grolimund, D.; Kaiser, M.; Borca, C. N.; Ingold, G.; Abela, R.; Chergui, M. Femtosecond XANES Study of the Light-Induced Spin Crossover Dynamics in an Iron(II) Complex. *Science* **2009**, *323*, 489–492.

(8) Consani, C.; Prémont-Schwarz, M.; ElNahhas, A.; Bressler, C.; van Mourik, F.; Cannizzo, A.; Chergui, M. Vibrational Coherences and Relaxation in the High-Spin State of Aqueous $[Fe^{II}(bpy)_3]^{2+}$. *Angew. Chem. Int. Ed.* **2009**, *48*, 7184–7187.

(9) Zhang, W.; Alonso-Mori, R.; Bergmann, U.; Bressler, C.; Chollet, M.; Galler, A.; Gawelda, W.; Hadt, R. G.; Hartsock, R. W.; Kroll, T.; Kjær, K. S.; Kubiček, K.; Lemke, H. T.; Liang, H. W.; Meyer, D. A.; Nielsen, M. M.; Purser, C.; Robinson, J. S.; Solomon, E. I.; Sun, Z.; Sokaras, D.; van Driel, T. B.; Vankó, G.; Weng, T.-C.; Zhu, D.; Gaffney, K. J. Tracking Excited-State Charge and Spin Dynamics in Iron Coordination Complexes. *Nature* **2014**, *509*, 345–348.

(10) Auböck, G.; Chergui, M. Sub-50-fs Photoinduced Spin Crossover in $[Fe(bpy)_3]^{2+}$. *Nat. Chem.* **2015**, *7*, 629–633.

(11) Moguilevski, A.; Wilke, M.; Grell, G.; Bokarev, S. I.; Aziz, S. G.; Engel, N.; Raheem, A. A.; Kühn, O.; Kiyan, I. Y.; Aziz, E. F. Ultrafast Spin Crossover in $[Fe^{II}(bpy)_3]^{2+}$: Revealing Two Competing Mechanisms by Extreme Ultraviolet Photoemission Spectroscopy. *ChemPhysChem* **2017**, *18*, 465–469.

(12) Lemke, H. T.; Kjær, K. S.; Hartsock, R.; van Driel, T. B.; Chollet, M.; Glownia, J. M.; Song, S.; Zhu, D.; Pace, E.; Matar, S. F.; Nielsen, M. M.; Benfatto, M.; Gaffney, K. J.; Collet, E.; Cammarata, M. Coherent Structural Trapping through Wave Packet Dispersion during Photoinduced Spin State Switching. *Nat. Commun.* **2017**, *8*, 15342.

(13) Kjær, K. S.; Van Driel, T. B.; Harlang, T. C. B.; Kunnus, K.; Biasin, E.; Ledbetter, K.; Hartsock, R. W.; Reinhard, M. E.; Koroidov, S.; Li, L.; Laursen, M. G.; Hansen, F. B.; Vester, P.; Christensen, M.; Haldrup, K.; Nielsen, M. M.; Dohn, A. O.; Pápai, M. I.; Møller, K. B.; Chabera, P.; Liu, Y.; Tatsuno, H.; Timm, C.; Jarenmark, M.; Uhlig, J.; Sundstöm, V.; Wärnmark, K.; Persson, P.; Németh, Z.; Szemes, D. S.; Bajnóczi, É.; Vankó, G.; Alonso-Mori, R.; Glownia, J. M.; Nelson, S.; Sikorski, M.; Sokaras, D.; Canton, S. E.; Lemke, H. T.; Gaffney, K. J. Finding Intersections between Electronic Excited State Potential Energy Surfaces with Simultaneous Ultrafast X-ray Scattering and Spectroscopy. *Chem. Sci.* **2019**, *10*, 5749–5760.

(14) de Graaf, C.; Sousa, C. Study of the Light-Induced Spin Crossover Process of the [Fe^{II}(bpy)$_3$]$^{2+}$ Complex. *Chem. Eur. J.* **2010**, *16*, 4550–4556.

(15) de Graaf, C.; Sousa, C. On the Role of the Metal-to-Ligand Charge Transfer States in the Light-Induced Spin Crossover in Fe^{II}(bpy)$_3$. *Int. J. Quantum Chem.* **2011**, *111*, 3385–3393.

(16) Sousa, C.; de Graaf, C.; Rudavskyi, A.; Broer, R.; Tatchen, J.; Etinski, M.; Marian, C. M. Ultrafast Deactivation Mechanism of the Excited Singlet in the Light-Induced Spin Crossover of [Fe(2,2′-bipyridine)$_3$]$^{2+}$. *Chem. Eur. J.* **2013**, *19*, 17541–17551.

(17) Domingo, A.; Sousa, C.; de Graaf, C. The Effect of Thermal Motion on the Electron Localization in Metal-to-Ligand Charge Transfer Excitations in [Fe(bpy)$_3$]$^{2+}$. *Dalton Trans.* **2014**, *43*, 17838–17846.

(18) Sousa, C.; Llunell, M.; Domingo, A.; de Graaf, C. Theoretical Evidence for the Direct ^{3}MLCT-HS Deactivation in the Light-Induced Spin Crossover of Fe(II)–Polypyridyl Complexes. *Phys. Chem. Chem. Phys.* **2018**, *20*, 2351–2355.

(19) Chang, J.; Fedro, A. J.; van Veenendaal, M. Ultrafast Cascading Theory of Intersystem Crossings in Transition-Metal Complexes. *Phys. Rev. B* **2010**, *82*, 075124.

(20) Baker, W.; van Veenendaal, M. Theory of Ultrafast Photoinduced Low-to-High Spin Crossover in Divalent Iron Systems. *Phys. Rev. B* **2021**, *104*, 014407.

(21) Zobel, J. P.; González, L. The Quest to Simulate Excited-State Dynamics of Transition Metal Complexes. *JACS Au* **2021**, *1*, 1116–1140.

(22) Zobel, J. P.; Heindl, M.; Plasser, F.; Mai, S.; González, L. Surface Hopping Dynamics on Vibronic Coupling Models. *Acc. Chem. Res.* **2021**, *54*, 3760–3771.

(23) Rozgonyi, T.; Vankó, G.; Pápai, M. Branching Mechanism of Photoswitching in an

Fe(II) Polypyridyl Complex Explained by Full Singlet-Triplet-Quintet Dynamics. *Commun. Chem.* **2023**, *6*, 7.

(24) Iuchi, S.; Morita, A.; Kato, S. Potential Energy Surfaces and Dynamics of Ni^{2+} Ion Aqueous Solution: Molecular Dynamics Simulation of the Electronic Absorption Spectrum. *J. Chem. Phys.* **2004**, *121*, 8446–8457.

(25) Iuchi, S. A Model Electronic Hamiltonian to Study Low-Lying Electronic States of $[Fe(bpy)_3]^{2+}$ in Aqueous Solution. *J. Chem. Phys.* **2012**, *136*, 064519.

(26) Iuchi, S.; Koga, N. An Improved Model Electronic Hamiltonian for Potential Energy Surfaces and Spin–Orbit Couplings of Low-Lying d–d States of $[Fe(bpy)_3]^{2+}$. *J. Chem. Phys.* **2014**, *140*, 024309.

(27) Iuchi, S.; Koga, N. Insight into the Light-Induced Spin Crossover of $[Fe(bpy)_3]^{2+}$ in Aqueous Solution from Molecular Dynamics Simulation of d–d Excited States. *Phys. Chem. Chem. Phys.* **2016**, *18*, 4789–4799.

(28) Iuchi, S.; Koga, N. A Model Electronic Hamiltonian to Describe Low-Lying d–d and Metal-to-Ligand Charge-transfer Excited States of $[Fe(bpy)_3]^{2+}$. *J. Comput. Chem.* **2021**, *42*, 166–179.

(29) Bhattacharyya, S.; Alías-Rodríguez, M.; Huix-Rotllant, M. Ultrafast Spin Crossover Photochemical Mechanism in $[Fe^{II}(2,2'–bipyridine)_3]^{2+}$ Revealed by Quantum Dynamics. *ChemRxiv* **2023**, DOI: `10.26434/chemrxiv-2022-q8hhp-v2`.

(30) Wang, J.; Wolf, R. M.; Caldwell, J. W.; Kollman, P. A.; Case, D. A. Development and Testing of a General Amber Force Field. *J. Comput. Chem.* **2004**, *25*, 1157–1174.

(31) Mai, S.; Marquetand, P.; González, L. Surface Hopping Molecular Dynamics. In *Quantum Chemistry and Dynamics of Excited States*; González, L., Lindh, R., Eds.; John Wiley & Sons, Ltd, 2020; pp 499–530.

(32) Mai, S.; Marquetand, P.; González, L. A General Method to Describe Intersystem Crossing Dynamics in Trajectory Surface Hopping. *Int. J. Quantum Chem.* **2015**, *115*, 1215–1231.

(33) Mai, S.; Marquetand, P.; González, L. Nonadiabatic Dynamics: The SHARC Approach. *WIREs Comput. Mol. Sci.* **2018**, *8*, e1370.

(34) Granucci, G.; Persico, M.; Toniolo, A. Direct Semiclassical Simulation of Photochemical Processes with Semiempirical Wave Functions. *J. Chem. Phys.* **2001**, *114*, 10608–10615.

(35) Ruckenbauer, M.; Barbatti, M.; Müller, T.; Lischka, H. Nonadiabatic Excited-State Dynamics with Hybrid ab Initio Quantum-Mechanical/Molecular-Mechanical Methods: Solvation of the Pentadieniminium Cation in Apolar Media. *J. Phys. Chem. A* **2010**, *114*, 6757–6765.

(36) Barbatti, M.; Granucci, G.; Persico, M.; Ruckenbauer, M.; Vazdar, M.; Eckert-Maksić, M.; Lischka, H. The On-the-Fly Surface-Hopping Program System Newton-X: Application to ab Initio Simulation of the Nonadiabatic Photodynamics of Benchmark Systems. *J. Photochem. Photobiol. A-Chem.* **2007**, *190*, 228–240.

(37) Granucci, G.; Persico, M.; Zoccante, A. Including Quantum Decoherence in Surface Hopping. *J. Chem. Phys.* **2010**, *133*, 134111.

(38) Smith, W.; Forester, T. R. DL_POLY_2.0: A General-Purpose Parallel Molecular Dynamics Simulation Package. *J. Mol. Graphics* **1996**, *14*, 136–141.

(39) Zobel, J. P.; Knoll, T.; González, L. Ultrafast and Long-Time Excited State Kinetics of an NIR-Emissive Vanadium(III) Complex II. Elucidating Triplet-to-Singlet Excited-State Dynamics. *Chem. Sci.* **2021**, *12*, 10791–10801.